

## A lower to middle Eocene astrochronology for the Mentelle Basin (Australia) and its implications for the geologic time scale

Vahlenkamp, Maximilian ; De Vleeschouwer, David; Batenburg, Sietske; Edgar, Kirsty; Hanson, Emma; Martinez, Mathieu; Paelike, Heiko; MacLeod, Kenneth; Li, Yong-Xiang; Richter, Carl; Bogus, Kara; Hobbs, Richard; Huber, Brian; Expedition 369 Scientific Participants

DOI:

[10.1016/j.epsl.2019.115865](https://doi.org/10.1016/j.epsl.2019.115865)

License:

Creative Commons: Attribution-NonCommercial-NoDerivs (CC BY-NC-ND)

*Document Version*

Publisher's PDF, also known as Version of record

*Citation for published version (Harvard):*

Vahlenkamp, M, De Vleeschouwer, D, Batenburg, S, Edgar, K, Hanson, E, Martinez, M, Paelike, H, MacLeod, K, Li, Y-X, Richter, C, Bogus, K, Hobbs, R, Huber, B & Expedition 369 Scientific Participants 2020, 'A lower to middle Eocene astrochronology for the Mentelle Basin (Australia) and its implications for the geologic time scale', *Earth and Planetary Science Letters*, vol. 529, 115865. <https://doi.org/10.1016/j.epsl.2019.115865>

[Link to publication on Research at Birmingham portal](#)

### **Publisher Rights Statement:**

Checked for eligibility: 10/10/2019

### **General rights**

Unless a licence is specified above, all rights (including copyright and moral rights) in this document are retained by the authors and/or the copyright holders. The express permission of the copyright holder must be obtained for any use of this material other than for purposes permitted by law.

- Users may freely distribute the URL that is used to identify this publication.
- Users may download and/or print one copy of the publication from the University of Birmingham research portal for the purpose of private study or non-commercial research.
- User may use extracts from the document in line with the concept of 'fair dealing' under the Copyright, Designs and Patents Act 1988 (?)
- Users may not further distribute the material nor use it for the purposes of commercial gain.

Where a licence is displayed above, please note the terms and conditions of the licence govern your use of this document.

When citing, please reference the published version.

### **Take down policy**

While the University of Birmingham exercises care and attention in making items available there are rare occasions when an item has been uploaded in error or has been deemed to be commercially or otherwise sensitive.

If you believe that this is the case for this document, please contact [UBIRA@lists.bham.ac.uk](mailto:UBIRA@lists.bham.ac.uk) providing details and we will remove access to the work immediately and investigate.



# A lower to middle Eocene astrochronology for the Mentelle Basin (Australia) and its implications for the geologic time scale

Maximilian Vahlenkamp<sup>a,\*</sup>, David De Vleeschouwer<sup>a</sup>, Sietske J. Batenburg<sup>b,c</sup>, Kirsty M. Edgar<sup>d</sup>, Emma Hanson<sup>d</sup>, Mathieu Martinez<sup>c</sup>, Heiko Pälike<sup>a</sup>, Kenneth G. MacLeod<sup>e</sup>, Yong-Xiang Li<sup>f</sup>, Carl Richter<sup>g</sup>, Kara Bogus<sup>h,i</sup>, Richard W. Hobbs<sup>j</sup>, Brian T. Huber<sup>k</sup>, Expedition 369 Scientific Participants<sup>l</sup>

<sup>a</sup> MARUM – Center for Marine and Environmental Sciences, University of Bremen, Klagenfurter Straße 2–4, Bremen, 28359, Germany

<sup>b</sup> Department of Earth Sciences, University of Oxford, South Parks Road, Oxford, OX1 3AN, United Kingdom

<sup>c</sup> Géosciences Rennes, UMR 6118, Université de Rennes 1, 35042 Rennes, France

<sup>d</sup> School of Geography, Earth and Environmental Sciences, University of Birmingham, Aston Webb Building Block A, Edgbaston B15 2TT, United Kingdom

<sup>e</sup> Department of Geological Sciences, University of Missouri, Columbia, 101 Geological Sciences Building, Columbia, MO 65211, USA

<sup>f</sup> School of Earth Sciences and Engineering, Nanjing University, 163 Xianlin Avenue, Nanjing 210046, PR China

<sup>g</sup> School of Geosciences, University of Louisiana at Lafayette, 611 McKinley Street, Lafayette, LA 70504, USA

<sup>h</sup> International Ocean Discovery Program, Texas A&M University, 1000 Discovery Drive, College Station, TX 77845-9547, USA

<sup>i</sup> Camborne School of Mines, College of Engineering, Mathematics and Physical Sciences, University of Exeter, Penryn, Cornwall, TR10 9FE, United Kingdom

<sup>j</sup> Department of Earth Sciences, University of Durham, Durham, DH1 3LE, United Kingdom

<sup>k</sup> National Museum of Natural History, Smithsonian Institution, MRC: NHB 121, 10th and Constitution Avenue NW, Washington, DC 20560, USA

## ARTICLE INFO

### Article history:

Received 31 July 2019

Received in revised form 24 September 2019

Accepted 26 September 2019

Available online xxx

Editor: I. Halevy

### Keywords:

Eocene

astrochronology

astronomical forcing

IODP 369

Mentelle Basin

## ABSTRACT

The geologic time scale for the Cenozoic Era has been notably improved over the last decades by virtue of integrated stratigraphy, combining high-resolution astrochronologies, biostratigraphy and magnetostratigraphy with high-precision radioisotopic dates. However, the middle Eocene remains a weak link. The so-called “Eocene time scale gap” reflects the scarcity of suitable study sections with clear astronomically-forced variations in carbonate content, primarily because large parts of the oceans were starved of carbonate during the Eocene greenhouse. International Ocean Discovery Program (IODP) Expedition 369 cored a carbonate-rich sedimentary sequence of Eocene age in the Mentelle Basin (Site U1514, offshore southwest Australia). The sequence consists of nannofossil chalk and exhibits rhythmic clay content variability. Here, we show that IODP Site U1514 allows for the extraction of an astronomical signal and the construction of an Eocene astrochronology, using 3-cm resolution X-Ray fluorescence (XRF) core scans. The XRF-derived ratio between calcium and iron content (Ca/Fe) tracks the lithologic variability and serves as the basis for our U1514 astrochronology. We present a 16 million-year-long (40–56 Ma) nearly continuous history of Eocene sedimentation with variations paced by eccentricity and obliquity. We supplement the high-resolution XRF data with low-resolution bulk carbon and oxygen isotopes, recording the long-term cooling trend from the Paleocene-Eocene Thermal Maximum (PETM – ca. 56 Ma) into the middle Eocene (ca. 40 Ma). Our early Eocene astrochronology corroborates existing chronologies based on deep-sea sites and Italian land sections. For the middle Eocene, the sedimentological record at U1514 provides a single-site geochemical backbone and thus offers a further step towards a fully integrated Cenozoic geologic time scale at orbital resolution.

© 2019 The Author(s). Published by Elsevier B.V. This is an open access article under the CC BY-NC-ND license (<http://creativecommons.org/licenses/by-nc-nd/4.0/>).

## 1. Introduction

Eocene climate is characterized by a long-term cooling trend after the extreme greenhouse conditions of the early Eocene, the

warmest climate state of the Cenozoic Era. During the middle and late Eocene, global climate shifts in a stepwise manner from the early Cenozoic greenhouse into an icehouse world (Zachos et al., 2008). This climate transition was accompanied by decreases in greenhouse gas concentrations, changes in precipitation patterns, carbon cycle shifts, and a number of transient warming events or “hyperthermals” paced by astronomical forcing (e.g. Cramer et al., 2003; Lourens et al., 2005; Westerhold et al., 2007, 2008, 2017;

\* Corresponding author.

E-mail address: [mvahlenkamp@marum.de](mailto:mvahlenkamp@marum.de) (M. Vahlenkamp).

<sup>1</sup> <https://iodp.tamu.edu/scienceops/precruise/swaustralia/participants.html>.

Sexton et al., 2011; Turner et al., 2014; Anagnostou et al., 2016; Lauretano et al., 2016; Westerhold et al., 2017). The short-lived hyperthermal events are associated with negative  $\delta^{13}\text{C}$  excursions interpreted to represent the injection of isotopically light carbon into the atmosphere and ocean and are linked with large parts of the ocean floor being the starved of carbonate (e.g. Kennett and Stott, 1991; Dickens et al., 1995; Zachos et al., 2005; Stap et al., 2010; Littler et al., 2014; Westerhold et al., 2017).

Constraining the rate and pace of past climate change is essential to disentangle the nature and drivers of past climate change. Over the past decades, the analysis of astronomically-forced climate cycles recorded in sedimentary sections has advanced our understanding of celestial mechanics and climate dynamics. Substantial progress in the understanding of celestial mechanics, i.e. the calculation of astronomical solutions back in time (e.g. Berger and Loutre, 1991; Laskar et al., 2004, 2011; Zeebe, 2017), and the analysis of the expression of the astronomic imprint in marine stratigraphic records led to the establishment of astronomical tuning methods as a standard technique for the Neogene time scale resulting in Neogene chronostratigraphies with only minor uncertainties (Gradstein et al., 2012; Hinnov and Hilgen, 2012). From here, the astronomical time scale (ATS) was extended into the Paleogene. An astronomical time scale for the Oligocene (Pälike et al., 2006) and across the Eocene-Oligocene Transition, with consistent results between different authors (Pälike et al., 2006; Westerhold et al., 2014), stretches into the youngest part of the middle Eocene.

For the middle Eocene, however, a lack of highly resolved sedimentary records has led to an “Eocene astronomical time scale gap”, which has hindered the establishment of a comprehensive astronomical time scale for the entire Cenozoic and led to substantial divergence between existing astrochronologies for the middle Eocene hampering their integration into the most recent fully-referenced Geologic Time Scale (GTS2012; Gradstein et al., 2012). GTS2012 uses a 6th-order polynomial fit for Chrons C13r through C23r to bridge the gap between the astronomical age models of the late Eocene (Pälike et al., 2006) and the early Eocene (Hilgen et al., 2010).

Subsequently, new and more detailed astronomical calibrations of the middle Eocene time scale were conducted based on deep-sea sediment cores recovered by the International Ocean Discovery Program (IODP) and its predecessors. Westerhold and Röhl (2013) and Westerhold et al. (2015) used the eccentricity signal in paleoclimatic records from Ocean Drilling Program (ODP) Site 1260 from the equatorial Atlantic and Hole 702B and Site 1263 in the South Atlantic to develop a new astrochronology for the poorly constrained interval of the middle Eocene (ca. 40–48 Ma). Boulila et al. (2018) later challenged the equatorial and south Atlantic chronologies and presented a conflicting middle Eocene astrochronology, based on sediments from the western North Atlantic (Sites U1408 and U1410). These North Atlantic drift deposits, however, lack a strong eccentricity imprint. Instead, their astrochronology is based on the stable  $\sim 173$ -kyr obliquity amplitude modulation recorded in the Ca/Fe ratio of sediments.

This difference in the orbital imprint between different stratigraphic sequences (eccentricity vs. obliquity) complicates the integration of results. However, Dinarès-Turell et al. (2018) recently constrained the age of the base of Chron C20n to  $\sim 43.5$  Ma. This result is consistent with the age of Westerhold et al. (2015) but in conflict with Boulila et al. (2018), who place this event at  $\sim 44.4$  Ma. Thus, magnetic reversal ages and chron durations for the middle Eocene “astronomical timescale gap” remain controversial. The early Eocene, in contrast, now features a coherent astrochronologic framework (Galeotti et al., 2017, 2019; Westerhold et al., 2017; Francescone et al., 2018). This framework is based on astronomical

tuning of globally distributed ocean drilling sites as well as land sections to the 405-kyr component in eccentricity.

The tuning process relies on accurate astronomical solutions that provide the precise astronomical configuration of the Earth at specific moments in geological history. The state-of-the-art eccentricity solutions (Laskar et al., 2011; Zeebe, 2017) agree with each other back to  $\sim 50$  Ma. Prior to 50 Ma, 100-kyr eccentricity cycles cannot be reliably reconstructed with the current astronomical models. Moreover, the timing of eccentricity nodes (minima in very long 2.4 Myr eccentricity) becomes ambiguous prior to 50 Ma, as they differ between solutions. Nonetheless, cyclostratigraphic techniques and astronomical tuning can still be instrumental in the early Eocene and Paleocene using the 405-kyr long eccentricity component as a tuning target (Lourens et al., 2005; Westerhold et al., 2007, 2008, 2017; Hilgen et al., 2010). The 405-kyr eccentricity cycle is extremely coherent between solutions and stable further back in time, making it the prime metronome for astrochronology in sequences older than 50 Ma (Laskar et al., 2004).

In this study, we present an astrochronology that spans the interval from the Paleocene Eocene Thermal Maximum (PETM,  $\sim 56$  Ma) into the middle Eocene ( $\sim 40$  Ma). The studied interval straddles the aforementioned “50-Ma boundary” forcing us to adopt different tuning strategies in the early and middle Eocene. This study uses the carbonate-rich Eocene sequences of recently recovered IODP Site U1514 in the Mentelle Basin (offshore southwest Australia) to pursue three major goals that are addressed in successive steps: First, we provide an early to middle Eocene astrochronology for IODP Site U1514 in the Mentelle Basin (southwest Australia). This astrochronologic framework is a valuable asset for future paleoceanographic studies in the region. Second, we compare the sedimentological record at U1514 to other middle Eocene astronomically tuned records to assess the inconsistencies between existing chronologies for the middle Eocene. Finally, we place the U1514 lower Eocene sedimentary sequence in the robust global astrochronological framework. This result will allow for the assessment of the fit between different astronomical solutions and geological data. A good fit between a specific solution and geological data indicates that this solution is more likely an accurate reflection of the evolution of solar system prior to 50 Ma, when the uncertainty in astronomical models increases drastically because of the chaotic behavior of our solar system (Laskar et al., 2004; Pälike et al., 2004; Ma et al., 2017). In other words, we reverse the traditional approach and try to constrain astronomical models by extracting the orbital signal from geological data.

## 2. Material and methods

### 2.1. Material

Site U1514 was the northernmost ( $33^\circ 7.2443'\text{S}$ ,  $113^\circ 5.4799'\text{E}$ ) and deepest (3850 m water depth) site drilled during IODP Expedition 369 in the Mentelle Basin (Fig. 1A) (Huber et al., 2019). The high paleolatitude ( $\sim 60^\circ\text{S}$  in at 50 Ma) of Site U1514 make the lithologic record a sensitive monitor of global climatic changes and deep-water circulation between mid and high latitudes. Site U1514 recovered 518.12 m of Cretaceous to Pleistocene sediments. The lower to middle Eocene interval at Site U1514 is recorded by  $\sim 145$  m (140–285 meter composite depth (mcd)) of carbonate-bearing (12–35 wt%) sediments with well-developed lithological alternations between lighter greenish gray clayey nannofossil chalk and darker nannofossil-rich claystone (Fig. 1E; Fig. 2) (Huber et al., 2019). The interval between 140 mcd and 196.06 mcd is present in Hole U1514A only. Below 196.06 mcd, there is a stratigraphic overlap between Holes U1514A and U1514C and we use the shipboard splice (Supplementary Tables 1, 2) from Holes U1514A and U1514C

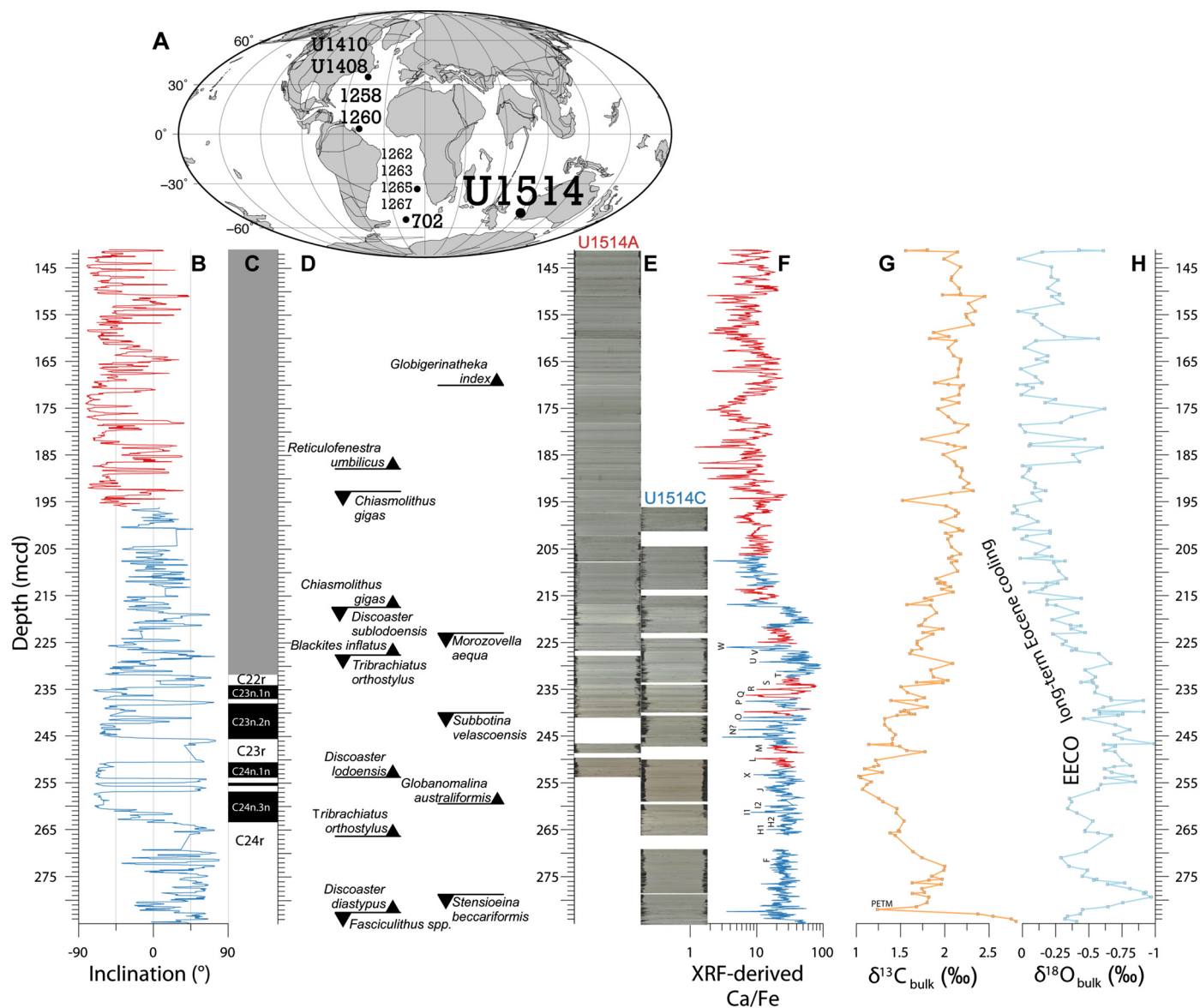


**Fig. 1.** (A) Location of Site U1514 and other deep-sea sites used for timescale reconstruction in the early and middle Eocene (paleomap ~45 Ma, [www.ods.de](http://www.ods.de)). (B) Downhole NRM20mT inclinations (after 20 mT demagnetization) from Holes U1514A (red) and U1514C (blue). (C) Magnetostratigraphic interpretation (white = normal, black = reversed, gray = undetermined). (D) Shipboard biostratigraphic events (Huber et al., 2019). (E) Core images stitched together with IODP CoreImage (Drury et al., 2018). (F) XRF-derived Ca/Fe ratio according to the shipboard splice between Holes U1514A (red) and U1514C (blue). Early Eocene hyperthermals follow the naming scheme of Cramer et al. (2003). (G–H) Bulk sediment carbon isotope and oxygen isotope data. (For interpretation of the colors in the figure(s), the reader is referred to the web version of this article.)

for the interval between ~196 and 259.6 mcd. The interval deeper than 253.82 mcd is present in Hole U1514C only (Fig. 1E).

## 2.2. Magnetostratigraphy

We used the natural remanent magnetization (NRM) inclinations measured on section-halves after 20 mT demagnetization treatment, i.e., NRM20mT, to define magnetic polarity (Huber et al., 2019). Paleomagnetic inclinations in the interval of 140–225 mcd are generally noisy and are thus not interpreted in this study (Fig. 1B). Towards the base of the section in Hole U1514C inclination values become less scattered and easier to interpret. The NRM20mT data allowed us to assign polarities for Chrons C22r–C24r, aided by the shipboard biostratigraphic constraints from the base of each core (Huber et al., 2019). We followed the shipboard magnetostratigraphic interpretation from 245.87 to 284 mcd. For the interval between ~230 and 245.87 mcd, we have revised the shipboard magnetostratigraphic interpretation. This reinterpretation

is necessary to ensure that the splice between Holes U1514A and U1514C and the magnetostratigraphy of these two holes are not in conflict. For example, the base of Chron C22r was offset by ~8 m between Hole U1514A and U1514C according to the shipboard interpretation. This offset is eliminated in our revised interpretation, as presented in Fig. 1. Chron boundary depths with differences to the shipboard magnetostratigraphic interpretation are given in Supplementary Table 3.

## 2.3. Biostratigraphy

Samples from Holes U1514A and U1514C core catchers and selected samples from split-core sections were analyzed for calcareous nannofossils and planktonic foraminifers. Calcareous nannofossil (T5 in Huber et al., 2019) and planktonic foraminiferal events (T6 in Huber et al., 2019) provide a first-order chronostratigraphic framework and allows for magnetostratigraphic interpretations (Huber et al., 2019).



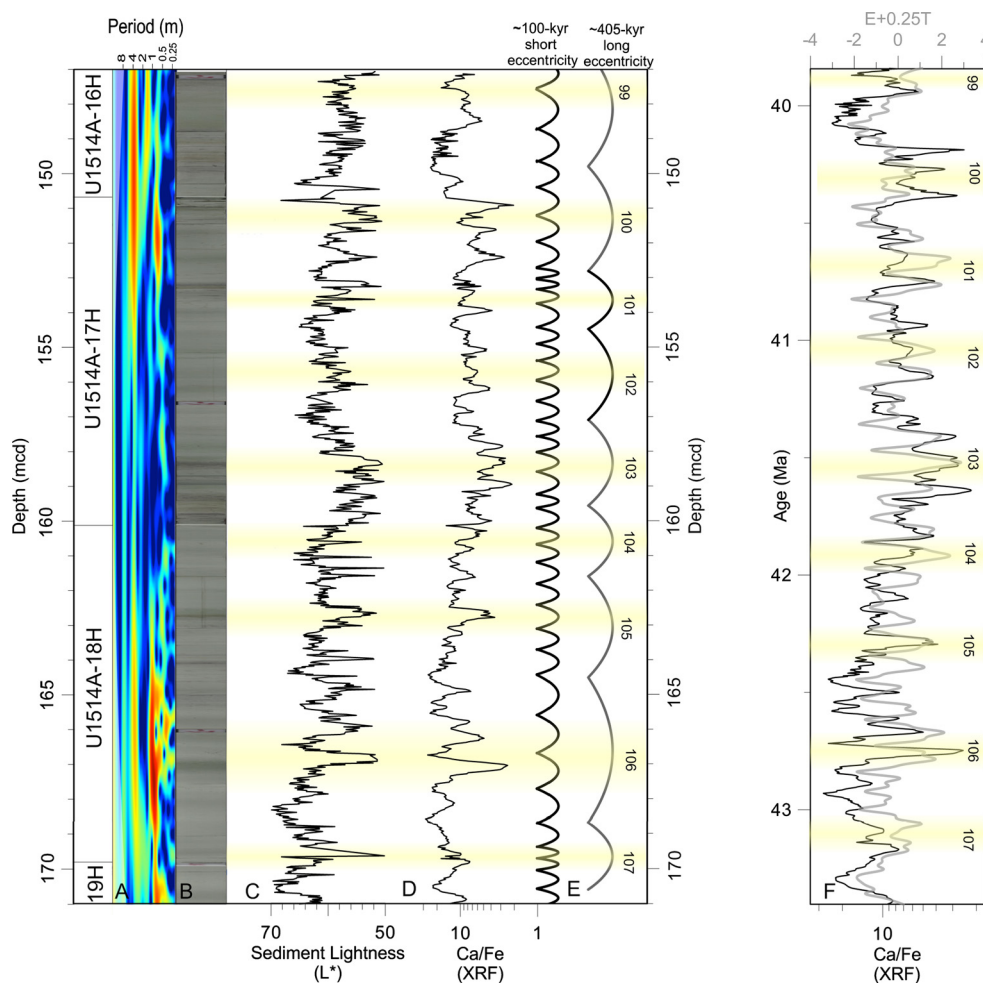


**Fig. 2.** Detailed relationship and cyclostratigraphic interpretation of lithology, colorimetry and geochemistry at Site U1514 in the interval between 147 and 171 mcd. (A) Wavelet analysis of the Ca/Fe record in the depth domain. (B) Core images (IODP CoreImage; Drury et al., 2018). (C) Sediment lightness ( $L^*$ ). (D) XRF-derived Ca/Fe ratio. (E) Cyclostratigraphic interpretation of the Ca/Fe depth-series. (F) Tuned XRF-derived Ca/Fe data plotted against the E+0.25T mix from La11/La04 (Laskar et al., 2004, 2011). Light yellow bands and numbers in C-F indicate 405-kyr eccentricity maxima. Supplementary Figs. 3–6 elucidate our cyclostratigraphic interpretations for the entire studied interval.

#### 2.4. X-ray fluorescence

The bulk elemental composition of U1514 sediments was measured on the split-core surfaces using the third-generation Avaatech XRF core scanner, located at the XRF Core Scanning Facility in the Gulf Coast Repository at Texas A&M University. Measurements were taken every 3 cm at a source energy of 10 kV (no filter, 0.16 mA) and a 6-seconds count time for each measurement. Element intensities were obtained by processing raw X-ray spectra using the iterative least-square software (bAxiL) package from Canberra Eurusys. In this study, we use the ratio between calcium and iron counts (Ca/Fe) to extract the imprint of astronomical forcing from the Eocene interval of the U1514 sedimentary archive. The Ca/Fe ratio tracks lithological variability, with higher Ca/Fe ratios in nanofossil chalks and lower Ca/Fe ratios in nanofossil-rich claystone.

#### 2.5. Bulk sediment carbon and oxygen isotopes

Bulk sediment samples of  $\sim 2 \text{ cm}^3$  were dried in a low temperature oven at  $50^\circ\text{C}$  overnight and then ground using an agate mortar and pestle to form a fine powder. The sample was homogenized and then  $\sim 150\text{--}250 \text{ }\mu\text{g}$  were used for isotope analysis. All bulk sediment stable carbon and oxygen isotope ( $\delta^{13}\text{C}$  and  $\delta^{18}\text{O}$ ) measurements were made on a GV Isoprime IR mass spectrometer with GV multiflow preparation line in the School of Geography,

Earth and Environmental Sciences at the University of Birmingham. Values are reported relative to the Vienna Pee Dee Belemnite (VPDB) standard. Stable isotope analyses have a typical analytical precision of  $0.06\text{‰}$  for  $\delta^{13}\text{C}$  and  $0.10\text{‰}$  for  $\delta^{18}\text{O}$  values. Bulk sediment stable carbon and oxygen isotope ( $\delta^{13}\text{C}$  and  $\delta^{18}\text{O}$ ) were measured in low resolution, insufficient to capture all shifts in carbon and oxygen isotope values associated with early Eocene hyperthermals, but the high-resolution XRF-derived Ca/Fe record allows us to observe the local sedimentary expression of hyperthermals in the Mentelle Basin.

#### 2.6. Time series analyses

Wavelet transforms of depth and time-series were carried out using the R-package “biwavelet” (Gouhier et al., 2016), which is based on the original wavelet program written by Torrence and Compo (1998). All other spectral analyses were carried out using the multitaper method (MTM) with three  $2\pi$ -tapers (Thomson, 1982) and conventional AR1 red noise modeling, as implemented in the R-package “astrochron” (Meyers, 2014). Depth-to-time conversion was carried out using function “tune” from the same R-package. With the function “bandpass” we employ frequency-selective filters between 0.002–0.003 cycles/kyr (500–333 kyr) to isolate and extract the component associated with 405-kyr eccentricity. To estimate the correlation between different data sets

**Table 1**

Comparison of Chron reversal ages in millions of years.

| Chron boundary  | CK95<br><i>Cande and Kent (1995)</i> | GTS2004<br><i>Ogg and Smith (2005)</i> | GTS2012<br><i>Gradstein et al. (2012)</i> | New Willwood<br><i>Tsukui and Clyde (2012)</i> | Atlantic<br><i>Westerhold et al. (2014, 2015)</i> | Ypresian ATS<br><i>Westerhold et al. (2017)</i> | Umbria-Marche<br><i>Francescone et al. (2018)</i> | U1514<br><i>This study</i> |
|-----------------|--------------------------------------|--|---|--|---|---|---|----------------------------|
| C22r/C23n.1n    | 50.778                               | 50.730                                 | 51.209                                    | 51.030   | 51.051  | 50.777  | 50.767  | 50.573                     |
| C23n.1n/23n.1r  | 50.946                               | 50.932                                 | 51.433                                    | 51.190   | 51.273  | 50.942  | 50.996  | 50.855                     |
| C23n.1r/C23n.2n | 51.047                               | 51.057                                 | 51.505                                    | 51.290   | 51.344  | 51.025  | 51.047  | 50.984                     |
| C23n.2n/C23r    | 51.743                               | 51.901                                 | 51.884                                    | 51.960   | 51.721  | 51.737  | 51.724  | 51.751                     |
| C23r/C24n.1n    | 52.364                               | 52.648                                 | 52.684                                    | 52.530   | 52.525  | 52.628  | 52.540  | 52.527                     |
| C24n.1n/C24n.1r | 52.663                               | 53.004                                 | 53.074                                    | 52.800   | 52.915  | 52.941  | 52.930  | 52.930                     |
| C24n.1r/C24n.2n | 52.757                               | 53.116                                 | 53.199                                    | 52.910   | 53.037  | 53.087  | 53.020  | 53.043                     |
| C24n.2n/C24n.2r | 52.801                               | 53.167                                 | 53.274                                    | 52.960   | 53.111  | 53.123  | 53.120  | 53.126                     |
| C24n.2r/C24n.3n | 52.903                               | 53.286                                 | 53.416                                    | 53.070   | 53.249  | 53.403  | 53.250  | 53.265                     |
| C24n.3n/C24r    | 53.347                               | 53.808                                 | 53.983                                    | 53.570   | 53.806  | 53.899  | 53.900  | 53.699                     |

and solutions and its statistical significance we use a nonparametric method by (Ebisuzaki, 1997). This method is implemented in the function 'surrogateCor' (Baddouh et al., 2016). The data with higher temporal resolution was resampled on the sample grid of the data with lower temporal resolution, using piecewise linear interpolation. Subsequently, the Pearson correlation coefficient ( $r$ ) is calculated. Next, the 'surrogateCor' function carries out the same correlation analyses for 10,000 Monte Carlo simulations, using phase-randomized surrogates. The surrogates are subject to the same interpolation process and compensate for the autocorrelation that characterize both time-series. To determine a  $p$ -value for the correlation, the Pearson correlation coefficient of the data is then compared to the distribution of correlation coefficients obtained from the surrogates.

### 3. Results

The U1514 Ca/Fe ratio ranges between 1.5 and 31 in the studied interval and co-varies with sediment brightness ( $L^*$ ) (Fig. 2). In the lower Eocene, between ~218–282 mcd, Ca/Fe ratios fluctuate around 30, indicating high carbonate content. From ~230 to 215 mcd, the Ca/Fe ratio shifts to values ranging between 10 and 15 (Fig. 1F). From ~240 to 195 mcd, the low-resolution bulk sediment  $\delta^{18}\text{O}$  data (Fig. 1H) exhibit the characteristic long-term Eocene cooling trend from the early Eocene climatic optimum into the early middle Eocene (195–237 mcd), and from 195 mcd upwards, the trend towards higher  $\delta^{18}\text{O}$  values ceases. Superimposed on the long-term trends of the geochemical records are a series of abrupt excursions to lower Ca/Fe values, which are associated with intervals of reduced wt%  $\text{CaCO}_3$  content. These sedimentological shifts are characteristic of early Eocene hyperthermals, which appear well expressed at Site U1514 (Fig. 1F).

#### 3.1. Cyclostratigraphic interpretation

The lithologic variations between 150 and 284 mcd at Site U1514 consist of alternations between light greenish gray, nannofossil chalk and clay-rich, darker nannofossil chalk (Huber et al., 2019). In other words, the lithological alternations are marked by quasi-cyclic variations in lightness and carbonate content. Shipboard colorimetric and XRF-derived Ca/Fe ratios closely track this rhythm in lithological properties (Fig. 2). First-order quasi-cyclic variations between lighter and darker sediments occur typically on sub-meter scale (Fig. 2). Very dark bands reoccur in intervals of about 3 to 5 m. The shipboard age model provides an approximate duration of 15.24 Ma for the interval between 136.67 mcd (*T. Chiasmolithus solitus*) and 281.80 mcd (*T. Fasciculithus* spp.) (Huber et al., 2019). This initial time constraint translates to an average sedimentation rate of ~0.95 cm/kyr throughout the entire studied interval. Hence, the first-order alternations in lithology (<1 m) are more likely to correspond to the geological expression of obliquity

or 100-kyr eccentricity, while the rhythm of darker layers (~3–5 m) may correspond to the influence of 405-kyr eccentricity. Longer cycles of ~10–25 m are also evident in Ca/Fe ratio and modulate the darkness in darker layers, hence the amplitude of the 405-kyr eccentricity cycles, following our cyclostratigraphic interpretation. We thus associate the decameter-scale cycles with the ~2.4-Myr eccentricity cycle. Minima in the 2.4-Myr cycle, often referred to as nodes, mark the strong expression of 405-kyr eccentricity cycles. We employ these “nodes” as useful pinpoints to anchor our floating cyclostratigraphic framework in absolute time.

In addition to establishing the connection between lithological cycles and the astronomical parameters that drive them, astronomical tuning of the U1514 Ca/Fe record to the astronomical solution requires determination of the phase-relationship between eccentricity and the Ca/Fe proxy. We calculated the correlation between detrended  $\log(\text{Ca/Fe})$  (Lowess smoother; smoothing factor = 0.1) and low-resolution bulk  $\delta^{18}\text{O}$ . The Monte-Carlo based correlation assessment of two auto-correlated time-series indicates a positive correlation coefficient of  $r = 0.186$  ( $p$ -value 0.03). This statistically-significant relationship suggests that carbonate-poor intervals are associated with warmer climatic conditions (assuming minimal salinity or ice volume changes at this time and no great differences between lithologies in the extent of diagenetic overprinting of original ratios). Warmer global climates are favored under high-eccentricity and high-obliquity configurations (e.g. Hays et al., 1976; De Vleeschouwer et al., 2017; Vahlenkamp et al., 2018). The above reasoning implies that minima in Ca/Fe at U1514 should be tuned into maxima in eccentricity (and obliquity). This relationship agrees with the largest amplitude of variability in lithology, as indicated by the color reflectance and Ca/Fe records (Fig. 2), likely corresponding to the largest amplitude of the orbital forcing parameters. A strong positive correlation ( $r = 0.302$ ;  $p$ -value: <0.01) between  $\delta^{18}\text{O}$  and  $\delta^{13}\text{C}$  also allows us to link the carbonate poor intervals during warmer climatic conditions to the input of isotopically light carbon from other reservoirs into the ocean. This finding is of particular interest as it allows us to identify and globally correlate Eocene hyperthermals over large distance, thus, providing an additional framework to project our astrochronology onto existing records. The astronomically-calibrated magnetostratigraphic ages presented in Table 1 are the result of tuning the inverted Ca/Fe record of U1514 to the eccentricity solution La10c (Laskar et al., 2011).

#### 3.2. Astronomical tuning of U1514

We generated the U1514 astrochronologic timescale by splitting the record in two separate intervals: the middle Eocene interval between ~142 and 203 mcd and the lower Eocene interval between ~203 and 284 mcd. For the tuning of the middle Eocene interval, we used the full eccentricity solution. For the tuning of the lower Eocene sequence, we initially solely used the stable 405-kyr

eccentricity cycles as a tuning target. Indeed, the 405-kyr component is coherent in all available eccentricity solutions (Supplementary Fig. 1, Laskar et al., 2011). We then calculated correlation coefficients between the 405-kyr tuned  $\log(\text{Ca}/\text{Fe})$  at Site U1514 and different eccentricity solutions (La10a, La10b, La10c, La10d, La11). We found the strongest negative correlation ( $r = -0.178$ ) with La10c. Subsequently, we refined the lower Eocene tuning using the full eccentricity La10c solution as a target. Tie points for both the initial and the refined tunings are shown in Supplementary Fig. 2 and are provided in Supplementary Table 4.

### 3.2.1. Early Eocene

We used the C23n.2n/C23r chron boundary (245.87 mcd) as an anchor for our early Eocene tuning. This choice is motivated by four elements: (1) the C23n.2n/C23r magnetic reversal is sharp and well expressed at Site U1514; (2) The interpretation of this magnetic reversal is identical in the shipboard interpretation and our revised interpretation; (3) The reversal occurs in a 405-kyr eccentricity minimum at U1514, in the Atlantic and in the Umbria Marche sections; (4) The age estimates of Westerhold et al. (2017) (51.737 Ma) and Francescone et al. (2018) (51.724 Ma) for this reversal are identical within uncertainty. We tuned the expression of the 405-kyr eccentricity minimum in Ca/Fe close to this magnetostratigraphic boundary into the same 405-kyr minimum as Westerhold et al. (2017) and Francescone et al. (2018). This approach results in a magnetochron age of 51.751 Ma at U1514. From this anchor point, we adopted a 405-kyr eccentricity tuning approach up- and downward to obtain an astrochronology for the early Eocene. Between 204 and 284 mcd, we identified 20 405-kyr eccentricity cycles of 3–5 m thickness, which we tuned into cycles  $\text{ecc}_{120}$  to  $\text{ecc}_{139}$ , referring to the number of 405-kyr cycles back in time, starting from the present. Unfortunately, we miss the sedimentary expression of cycle  $\text{ecc}_{135}$  because of a recovery gap between  $\sim 266$  and  $269$  mcd. The age-depth model of the lower Eocene using the full La10c eccentricity solution is constrained by 39 tie-points. The sedimentation rate during the early Eocene (203–284 mcd) varied between  $\sim 0.5$  and  $2$  cm/kyr and averaged around  $1$  cm/kyr (Fig. 3), but was remarkably consistent between  $\sim 221$  and  $281$  mcd.

### 3.2.2. Middle Eocene

Our tuning approach in the middle Eocene exploits the stability of the current astronomical solutions over the past 50 Ma. In particular, the timing of the nodes in the  $\sim 2.4$ -Myr component of eccentricity is consistent between the different astronomical solutions in the middle Eocene. These nodes are minima in the  $\sim 2.4$ -Myr eccentricity cycle and characterized by strong expression of the 405-kyr eccentricity cycle and weak expression of short 100-kyr eccentricity. They are particularly well-expressed in the U1514 sedimentary record. Thus, they can be identified visually as long-lasting maxima in Ca/Fe that extend over several meters. In the wavelet transform, these intervals are marked by increased power in the 405-kyr eccentricity band and low power in the 100-kyr eccentricity band (Fig. 4). We used both indicators to identify the stratigraphic position of nodes in the  $\sim 2.4$  Myr eccentricity cycle:  $\sim 150$ ,  $\sim 170$ ,  $\sim 180$  and  $\sim 202$  mcd.

Building on our tuning for the lower Eocene, we tied these four nodes into those of the astronomical solution, beginning with the node centered at 202 mcd into the oldest stable eccentricity node around  $\text{ecc}_{119}$  (47.8 Ma). We subsequently tuned the following nodes at 180, 170 and 150 mcd into the respective nodes at cycles  $\text{ecc}_{112}$ ,  $\text{ecc}_{107}$  and  $\text{ecc}_{100}$  in the astronomical solution. We then refined the age model by first introducing additional tie points on the 405-kyr eccentricity level and then on the 100-kyr eccentricity level between 40 and 48.5 Ma. According to this tuning, intervals of extreme eccentricity correspond to the deposition of carbonate-

poor sediments at Site U1514. Our middle Eocene age model consists of 59 age-depth ties in the interval between 142 and 203 mcd. The lithological alternations in the middle Eocene of U1514 also reflect an important obliquity component, in particular near nodes in the  $\sim 2.4$  Myr eccentricity cycle, when the expression of 100-kyr eccentricity is weak. As a result of the recorded obliquity-eccentricity interactions we find that the U1514 Ca/Fe signal resembles the astronomic signature of an eccentricity+(0.25\*tilt) mix between 40 and 48 Ma (Fig. 2). Sedimentation rates during the middle Eocene varied between  $\sim 0.3$  and  $1.8$  cm/kyr and averaged around  $0.7$  cm/kyr.

## 4. Discussion

This work provides a detailed chronostratigraphic framework for future Eocene paleoclimatic studies at Site U1514. However, in this work, we also use Site U1514 to assess the inconsistencies between existing middle Eocene chronologies and to place the U1514 lower Eocene sedimentary sequence in a global astrochronological framework. To achieve these goals, an integration of our results with existing chronologies is crucial. Magnetostratigraphy provides independent temporal control between 234.73 and 261.56 mcd but is of ambiguous quality outside this interval. Nevertheless, we can correlate the lithological variations at U1514 with sedimentological and geochemical data from the Atlantic using chemostratigraphy. U1514 Ca/Fe data clearly exhibit early Eocene hyperthermals (Fig. 5) that we identified based on their stratigraphic position relative to magnetochron boundaries, their interrelation (bundling and amplitude) and their characteristic occurrence patterns (Figs. 5 and 6). The pattern of hyperthermals matches quite well between U1514, the Atlantic deep-sea sites and Italian land sections (Westerhold et al., 2017; Francescone et al., 2018). Using our integrated approach, we were able to identify all hyperthermals between the PETM (55.93 Ma) and hyperthermal “W” (49.58 Ma). Our chemostratigraphic correlation respects the magnetostratigraphic framework and follows the hyperthermal naming scheme of Cramer et al. (2003) (Figs. 1, 5, 6). Interestingly, compared to the Atlantic sites, the Mentelle Basin hyperthermals between 245 and 282 mcd (E2-L) have a relatively weak expression whereas those between 225 and 245 mcd (M-W) have a relatively strong expression (Fig. 5).

In the middle Eocene, distinct features, such as the shape of the node at 48 Ma, distinct maxima in Ca/Fe at U1514 46.9 Ma, as well as the position of the nodes and the lowest Ca/Fe allow a direct comparison of the U1514 Ca/Fe time-series to the proxy records of the Atlantic sites (Fig. 5). The similarity between South Atlantic shifts in stable carbon isotopes and the sedimentological and stable carbon isotope record in the Indian Ocean hints at the global nature of the climate perturbations on astronomical timescales that typify the early and middle Eocene (Fig. 5).

Biostratigraphy did not play a major role in the lower Eocene inter-basin correlations described above because the shipboard biostratigraphic events between 232 and 285 mcd have uncertainties of  $\sim 1$  Myr and internal inconsistencies of up to  $\sim 2$  Myr (i.e. 20 m in the depth-domain) (Huber et al., 2019). However, this interval is well-constrained by magnetostratigraphy and/or the hyperthermal chemostratigraphy.

The last occurrence (LO) of benthic foraminifera *Stensioeina beccariformis* is found in U1514C-11R-CC. This position is in accordance with the magnetostratigraphy (Chron C24r) and the relative position of the PETM slightly higher in the sediment column. In contrast, the first occurrence (FO) of the planktonic foraminifera *Globanomalina australiformis* occurs in U1514C-7R-CC, 37.5 m above the LO of *S. beccariformis*, yet globally the FO *G. australiformis* is recorded before the LO of *S. beccariformis*. This is likely because of



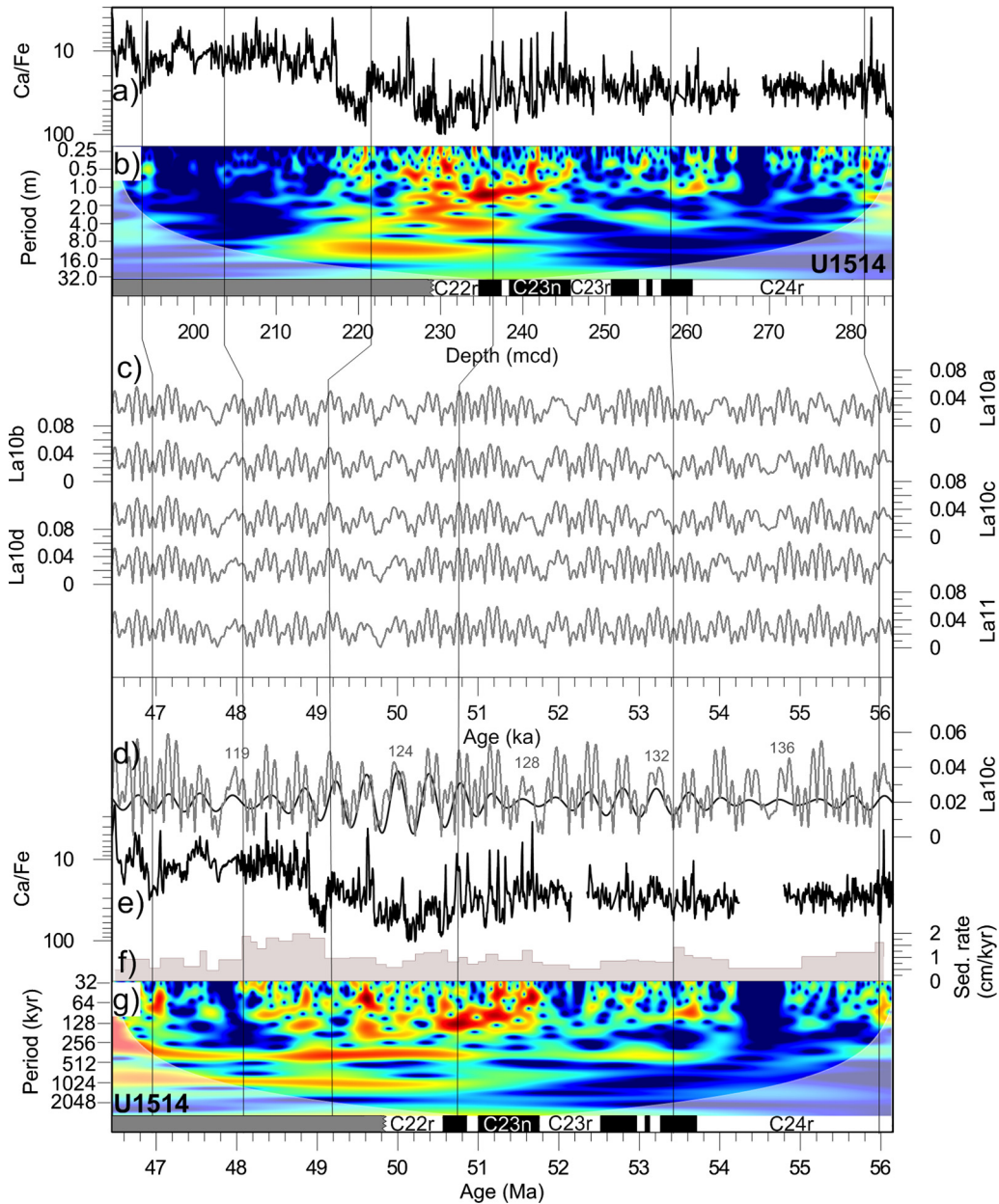


**Fig. 3.** Early Eocene astrochronology for IODP Site U1514. We show the interval between ~46.5 and 56 Ma. (A) Inverted Ca/Fe data from Site U1514 in the depth domain, (B) wavelet analysis of U1514 in the depth domain. (C) Orbital solutions La10a, La10b, La10c, La10d and La11 (Laskar et al., 2011). (D) Eccentricity bandpass filter of tuned time series of U1514 (black) over the astronomical solution La10c. (E) tuned Ca/Fe data from Site U1514 (F) sedimentation rate in U1514, (G) wavelet analysis of the tuned record from U1514.

the sporadic and rare occurrence of this species at Site U1514 in the early Eocene making the FO artificially high.

The LO of *Subbotina velascoensis* and *Morozovella aequa* in U1514C-7R-CC and U1514C-5R-CC, respectively, occur in C23n or younger in U1514. However, the position of these events is within C24r according to GTS2012.

Nannofossil events in the early Eocene are more consistent with the magnetostratigraphy and hyperthermals than planktonic foraminifera events but are still offset from GTS2012 ages by up to 1 Myr. The LO of *Tribachiatus orthostylus* in U1514A-28X-CC in our tuning between 49.87 and 50.84 is in excellent agreement with the assigned age of 50.5 Ma in the GTS2012. However, there is poor agreement between the U1514 ages for the FO of *Blackites inflata* and the LO of *Discoaster subloboensis* which appear older (between 48.85 and 49.69 Ma) than in the GTS2012 (events at 47.84 and 46.21 Ma, resp.). Despite this discrepancy, we have good confi-

dence in our early Eocene age model, as it is well constrained by the recognition of hyperthermal W based on the strong negative excursion in Ca/Fe ratios at 226.02 mcd. For the middle Eocene, the calculated age of all three nannofossil events (FO *Chiasmolithus gigas*, LO *Chiasmolithus gigas* and FO *Reticulofenestra umbilica*) at Site U1514 are offset by at least 1 Myrs from the GTS2012. On the other hand, the middle Eocene planktonic foraminiferal datum, LO *Globigerinathea index* occurs at the expected age according to GTS2012.

Despite mismatches between the numerical ages of biostratigraphic events in our U1514 age model and GTS2012, we do not doubt the magneto-, chemo-, and cyclostratigraphy presented in this study. Indeed, the latter three stratigraphic techniques are internally and mutually consistent. The low resolution of the ship-board biostratigraphic data (increasing the potential for sampling errors to have large effects), low diversity planktonic foraminifera



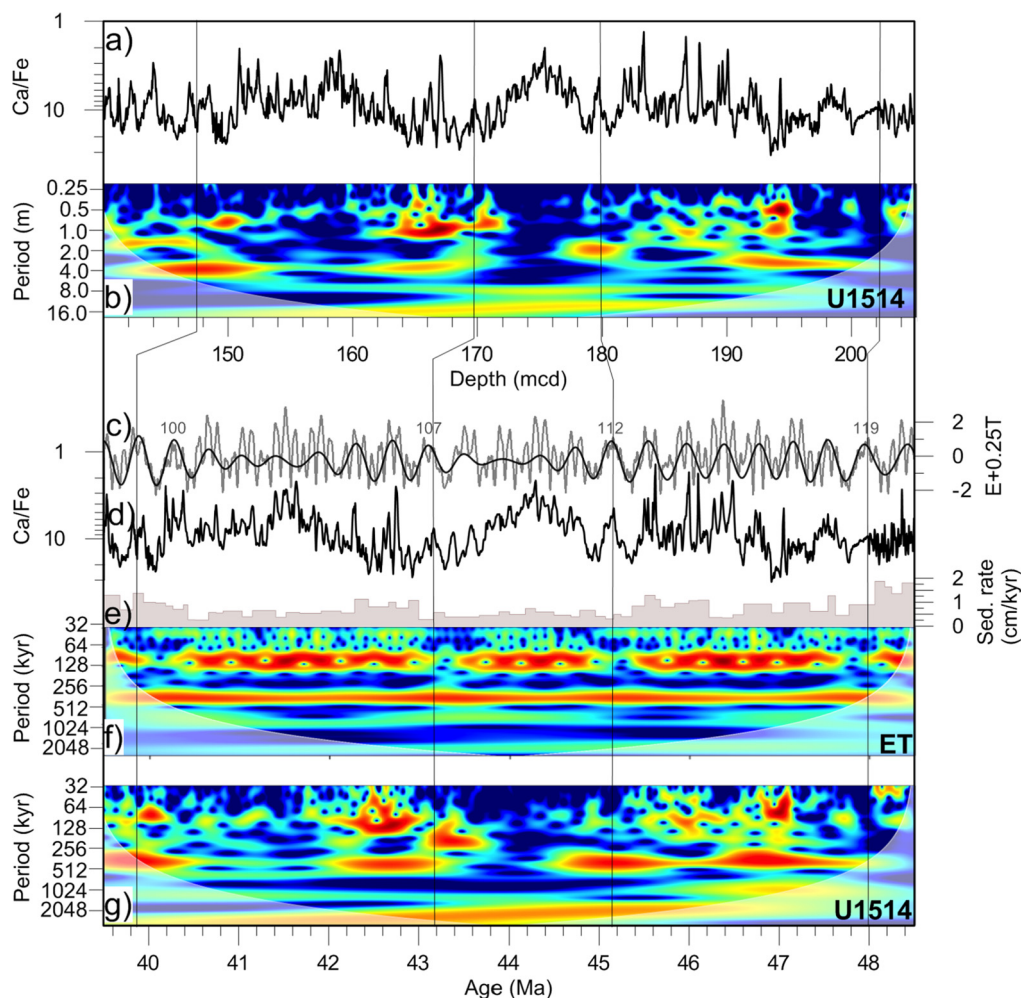


**Fig. 4.** Middle Eocene cyclostratigraphy for IODP Site U1514. We show the interval between  $\sim 39.5$  and  $48.5$  Ma. (A) Inverted Ca/Fe data from Site U1514 in the depth domain, (B) wavelet U1514 in the depth domain, (C) Eccentricity bandpass filter of tuned time series of U1514 (black) over orbital eccentricity+0.25tilt (grey) from La11 (eccentricity) and La04 (obliquity) solution (Laskar et al., 2004, 2011). Eccentricity bandpass filter of tuned time series of U1514 (black). Long eccentricity (405-kyr) cycle numbers relate to nodes in very long eccentricity ( $\sim 2.4$ -Myr). (D) tuned Ca/Fe data from Site U1514 (E) sedimentation rate in U1514. (F) Wavelet analysis of the eccentricity+0.25Tilt mix from La11 (eccentricity) and La04 (obliquity) and (G) wavelet analysis of the tuned record from U1514.

assemblages, known and unrecognized diachroneity in the biostratigraphic events between basins, and/or errors in the GTS2012 ages (Gradstein et al., 2012) likely explain existing mismatches. The strong independent age model at this site is promising for future high-resolution bioevent calibration.

We assess the uncertainty of our astrochronology by comparing the ages of the early Eocene hyperthermals between our U1514 record, the Atlantic deep-sea sites (Westerhold et al., 2017) and the Umbria/Marche sections (Francescone et al., 2018). We find a maximum offset of  $\sim 100$  kyr at hyperthermal M. This maximum offset is a good measure for the uncertainty on our tuning.

#### 4.1. Implications for the early Eocene GPTS

Five Atlantic deep-sea sites (Sites 1258, 1262, 1263, 1265, and 1267) with detailed cyclo-, bio-, chemo- and magnetostratigraphy constitute the geomagnetic polarity timescale (GPTS) for the early Eocene (Westerhold et al., 2017). Francescone et al. (2018) recently confirmed this geochronology on the level of 405-kyr eccentricity cycles using sections from central Italy (Table 1).

The U1514 astrochronology presented here suggests very similar durations for magnetochrons C23n.1n through C24n.3n (Table 2), as those reported by Westerhold et al. (2017) for the Atlantic composite. Inconsistencies do not exceed 200 kyr. The combined duration of Chrons C23n.1n, C23n.1r, and C23n.2n is 220 kyr

longer at U1514 compared to the Atlantic composite. Moreover, the age of hyperthermal O and of the C23n.2n/C23r reversal accord well between Sites U1514 and 1263. Our numerical ages for hyperthermals K (or ETM3) to H1 (or ETM2) match with the tuning of Westerhold et al. (2017). Therefore, we attribute the minor inconsistencies between the duration estimates of the subchrons within C24n to small uncertainties in the geomagnetic interpretations at U1514 and 1263.

Also, from a chemostratigraphic perspective, our early Eocene astrochronology agrees with previously published timescales. Indeed, age differences for the PETM and other early Eocene hyperthermals between U1514, on the one hand, and Westerhold et al. (2017) or Francescone et al. (2018), on the other hand, are generally less than 100 kyr (Table 3). It should be noted that we inferred all hyperthermals based on their carbonate-poor sedimentology, except for the PETM, for which the identification is directly based on its negative  $\delta^{13}\text{C}$  excursion (Fig. 1G). The PETM occurs at 55.87 Ma at Site U1514, in excellent agreement with the age reported by Westerhold et al., 2017. We thus confirm that the PETM is not linked to high eccentricity forcing, unlike the other Eocene hyperthermals.

The timing of the hyperthermals indicates that minor inconsistencies in the age of magnetic reversals between our study and Westerhold et al. (2017) could be explained by discrepancies in

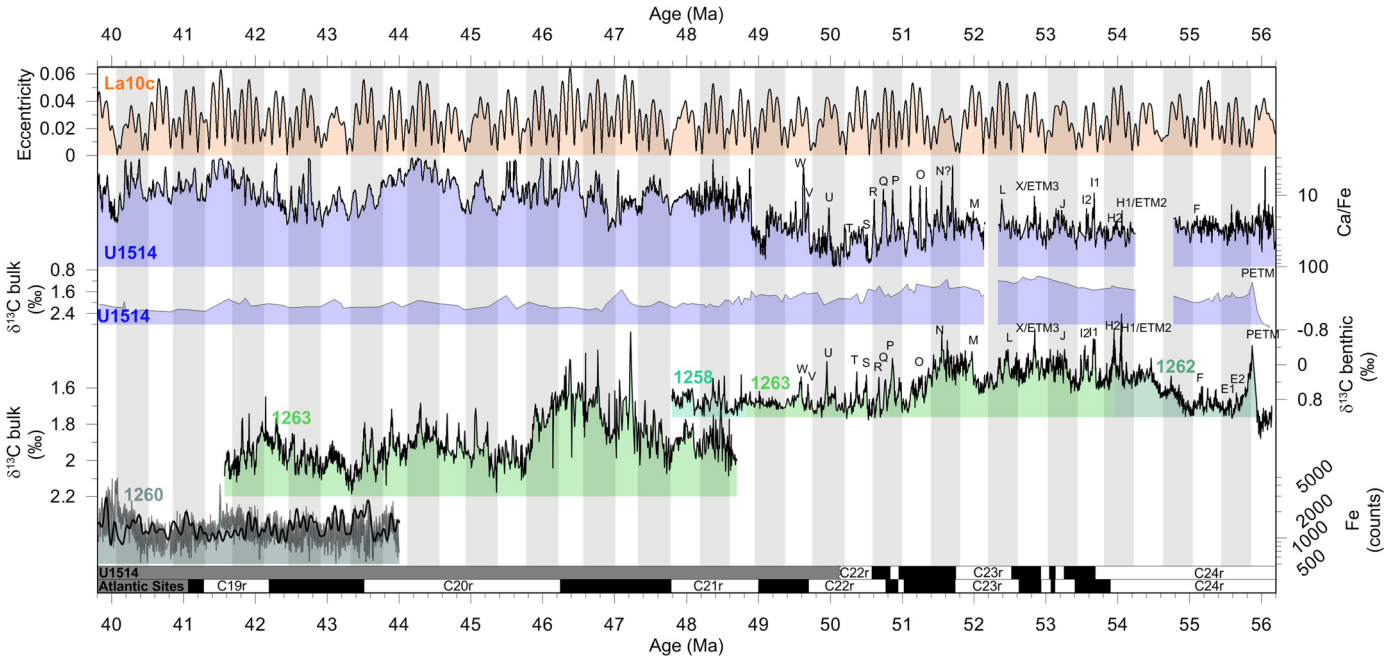


**Fig. 5.** Global astrochronologic framework for the early to middle Eocene. Comparison of the astrochronology at U1514 with Sites 1260 (Iron counts gray, precession amplitude black; Westerhold and Röhl, 2013), and 1258 ( $\delta^{13}\text{C}$  benthic; Sexton et al., 2011) from the equatorial Atlantic and Sites 1263 ( $\delta^{13}\text{C}$  bulk (Westerhold et al., 2015),  $\delta^{13}\text{C}$  benthic (Stap et al., 2010; Lauretano et al., 2015, 2016)), and 1262 ( $\delta^{13}\text{C}$  benthic; Stap et al., 2010; Littler et al., 2014) from Walvis Ridge. All age models for the Atlantic sites are according to Westerhold et al. (2017).

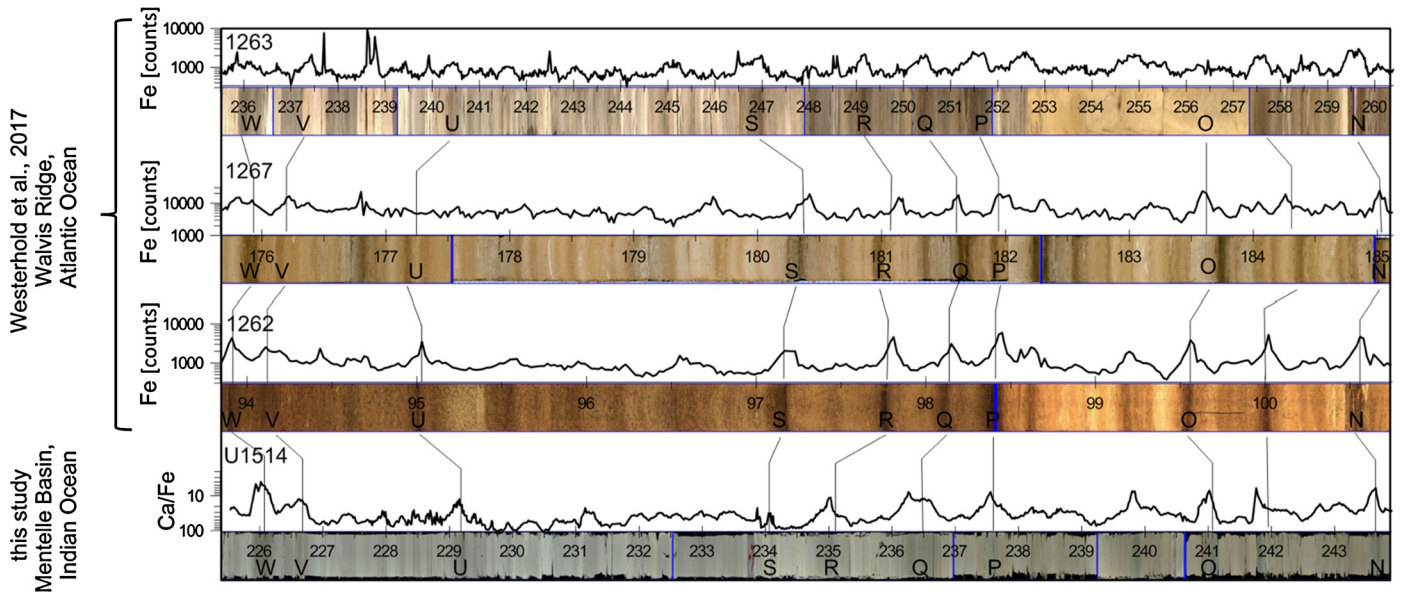


**Fig. 6.** Chemostratigraphic correlation between Atlantic Sites 1263, 1267, 1262 from Walvis Ridge and Site U1514 in the Mentelle Basin for the interval between hyperthermal "N" and hyperthermal "W". Hyperthermals are characterized by darker bands and increased iron counts at all sites. Spliced core images were created using IODP CoreImage (Drury et al., 2018).

the magnetostratigraphic interpretation of lower Eocene deep-sea sites (Fig. 3). The magnetostratigraphic framework of Westerhold et al. (2017) and Francescone et al. (2018) is based on multiple sites and land sections and is therefore arguably more robust than our single-site magnetostratigraphic interpretation of Chrons C22r through C24r. Furthermore, these authors age models result in more gradual variations in mid-ocean ridge spreading rates.

#### 4.2. Towards a consistent middle Eocene GPTS

The middle Eocene timescale (between C18r-C21n) is currently characterized by large uncertainties arising from less consistent ra-

dioisotopic dating and astrochronologies than the rest of the Cenozoic. A particular obstacle for the construction of a complete Cenozoic astronomical timescale is the considerable discrepancy between two recent astronomical age models for the middle Eocene (Westerhold et al., 2013, 2015; Boullila et al., 2018).

Site U1514 does not currently have a detailed and consistent magneto- or biostratigraphic framework for the middle Eocene. Nevertheless, U1514 yields the potential to evaluate the respective quality of competing chronologies that have been proposed as the backbone for the middle Eocene timescale. The resemblance of the Ca/Fe record at Site U1514 with sedimentological and geochemical data from the Atlantic (Fig. 5 and Fig. 7) allows com-

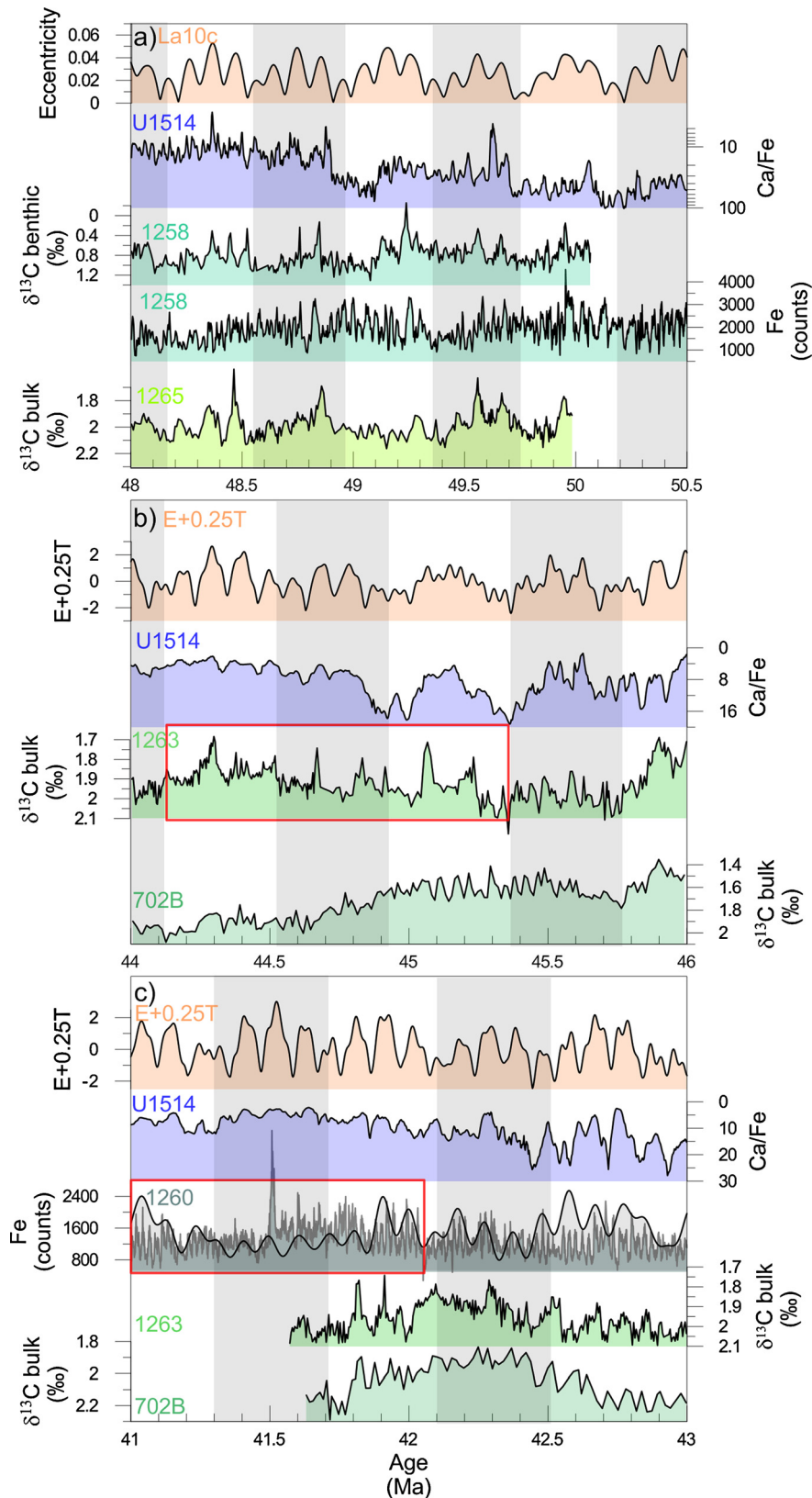


**Fig. 7.** Detailed comparison of the astrochronology at U1514 in the SE Indian Ocean with published astrochronologies from the Atlantic (Westerhold et al., 2013, 2015, 2017) in intervals not constrained by magnetostratigraphy at U1514. (A) Lower Eocene interval between 48 and 51 Ma. Note the similarities in particular between U1514 Ca/Fe and 1258 benthic  $\delta^{13}\text{C}$ . (B) Middle Eocene interval between 44 and 46 Ma. The red rectangle marks the interval where Boulila et al., 2018 suggested two instead of three 405-kyr cycles. Note that the lowest values in Fe coincide with the coolest orbital configuration and highest Fe values with the warmest astronomical configuration in both U1514 and 1263. (C) Middle Eocene interval between 41 and 43 Ma. The red square marks the interval characterized by a hiatus according to Boulila et al. (2018). Note that the highest Fe values in U1514 and 1260 occur during the C19r Event at 41.5 Ma and the similarity of the shape of individual 100-kyr cycles e.g. the cycle 42.6–42.75 Ma.



**Table 2**

Comparison of Chron durations in millions of years.

| Chron   | CK95<br><i>Cande and Kent<br/>(1995)</i> | GTS 2004<br><i>Ogg and Smith<br/>(2005)</i> | GTS2012<br><i>Gradstein et al.<br/>(2012)</i> | New Willwood<br><i>Tsukui and Clyde<br/>(2012)</i> | Atlantic<br><i>Westerhold et al.<br/>(2014, 2015)</i> | Ypresian ATS<br><i>Westerhold<br/>et al. (2017)</i> | Umbria-Marche<br><i>Francescone<br/>et al. (2018)</i> | U1514<br><i>This study</i> |
|---------|--|---|---|--|---|---|---|----------------------------|
| C23n.1n | 0.168                                    | 0.202                                       | 0.207   | 0.160  | 0.222   | 0.165   | 0.229   | 0.282                      |
| C23n.1r | 0.101                                    | 0.125                                       | 0.126   | 0.100  | 0.071   | 0.083   | 0.051   | 0.129                      |
| C23n.2n | 0.696                                    | 0.844                                       | 0.872   | 0.670  | 0.377   | 0.712   | 0.677   | 0.767                      |
| C23r    | 0.621                                    | 0.747                                       | 0.787   | 0.570  | 0.804   | 0.891   | 0.816   | 0.776                      |
| C24n.1n | 0.299                                    | 0.356                                       | 0.454   | 0.270  | 0.390   | 0.313   | 0.390   | 0.403                      |
| C24n.1r | 0.094                                    | 0.112                                       | 0.125   | 0.110  | 0.122   | 0.146   | 0.090   | 0.113                      |
| C24n.2n | 0.044                                    | 0.051                                       | 0.075   | 0.050  | 0.074   | 0.036   | 0.100   | 0.083                      |
| C24n.2r | 0.102                                    | 0.119                                       | 0.142   | 0.110  | 0.138   | 0.280   | 0.130   | 0.139                      |
| C24n.3n | 0.444                                    | 0.522                                       | 0.567   | 0.500  | 0.557   | 0.496   | 0.650   | 0.434                      |

**Table 3**

Overview of names and ages (Ma) of hyperthermal events identified in this study.

| Hyperthermal | Ypresian ATS<br><i>Westerhold et al.<br/>(2017)</i> | Umbria-Marche<br><i>Francescone et al.<br/>(2018)</i> | U1514<br><i>This study</i> |
|--------------|---|---|----------------------------|
| PETM         | 55.93 ± 0.06  | 56.10   | 55.87 ± 0.06               |
| E1           | 55.65   | –   | –                          |
| E2           | 55.56   | –   | –                          |
| F            | 55.17   | –   | 55.19                      |
| H1/ETM2      | 54.05   | 54.09   | 54.06                      |
| H2           | 53.95   | –   | 53.96                      |
| I1           | 53.67   | –   | 53.67                      |
| I2           | 53.55   | –   | 53.55                      |
| J            | 53.26   | –   | 53.22                      |
| K/ETM3       | 52.84   | 52.80   | 52.84                      |
| L            | 52.46   | 52.44   | 52.39                      |
| M            | 51.97   | 52.00   | 51.90                      |
| N            | 51.55   | 51.63   | 51.55                      |
| O            | 51.23   | 51.21   | 51.25                      |
| P            | 50.86   | 50.85   | 50.87                      |
| Q            | 50.76   | 50.76   | 50.73                      |
| R            | 50.67   | 50.62   | 50.60                      |
| S            | 50.48   | 50.40   | 50.47                      |
| T            | 50.37   | 50.29   | 50.28                      |
| U            | 49.95   | 49.96   | 49.95                      |
| V            | 49.68   | 49.67   | 49.63                      |
| W            | 49.58   | 49.53   | 49.51                      |

parison on the 405-kyr and even ~100-kyr eccentricity level. The big advantage of the middle Eocene section at U1514 is the excellent expression of the mix between obliquity and eccentricity and particularly the clearly expressed nodes in ~2.4-Myr eccentricity (Fig. 2). The interference between eccentricity and obliquity is quite characteristic, both in the astronomical solutions and in the sedimentological record (Fig. 2). This distinctness is particularly evident during nodes, which increases our confidence in the U1514 astrochronology.

Boulila et al. (2018) suggested an alternative interpretation to the astrochronology of Westerhold and Röhl (2013) and Westerhold et al. (2015). They reinterpreted the cyclostratigraphy at Site 1263 and Hole 702B by shortening Chron C20r by one 405-kyr cycle and proposed a 700-kyr-long hiatus in Chrons C19n and C19r at Site 1260. We, though, find a good correspondence between our astronomically tuned U1514 Ca/Fe and the  $\delta^{13}\text{C}$  time-series of Sites 1263 and 702 between cycle  $\text{ecc}_{107}$  to cycle  $\text{ecc}_{119}$ . This interbasal agreement between Sites U1514, 1263 and 702 suggests that the Westerhold et al. (2015) chronology is not compromised by data gaps and misinterpretations (Fig. 7B). Similar variability in proxy records of U1514 and 1260 in Chrons C19n–C19r provides additional support for the completeness of the stratigraphic record at 1260. Notwithstanding a lack of independent chronostratigraphic markers at U1514, the close correspondence of orbitally paced sedimentary patterns between Sites U1514 and 1260 strongly suggests that stratigraphic problems with the North Atlantic Sites U1408 and U1410 lie at the basis of the divergence be-

tween the competing middle Eocene chronologies. The problems at the North Atlantic Sites are likely due to the presence of hiatuses and slumps in these contourite drift deposits. Contourite drifts in general and the Newfoundland drifts in particular are associated with erosional features and slumping (e.g. Shanmugam, 2017; Van Peer et al., 2017). Furthermore, these drifts are characterized by substantial inter-hole variability, complicating cyclostratigraphic work (Van Peer et al., 2017; Vahlenkamp et al., 2018).

#### 4.3. Constraints for astronomic solutions

The sedimentological record of U1514 supports previous conclusions by Westerhold et al. (2017) suggesting that the La2010b/c eccentricity solutions in which the position of astronomical objects is based on the INPOP08 ephemeris (Fienga et al., 2009; Laskar et al., 2011) are most consistent with the geological data between 50–56 Ma. However, from an astronomer's point of view the La2010b/c solutions are considered less reliable than those which use the more accurate ephemeris INPOP10 (Fienga et al., 2011; Laskar et al., 2011). To evaluate the fit of the astronomical solutions to geological data, we calculated Pearson correlation coefficients between the U1514 log(Ca/Fe) record and all available astronomical solutions, for the interval between 56 and 50 Ma. The log(Ca/Fe) record correlates better with La2010b ( $r = -0.173$ ) and La2010c ( $r = -0.178$ ) than with La2010a ( $r = -0.154$ ), La2010d ( $r = -0.118$ ), La2011 ( $r = -0.102$ ) or the Zeebe (2017) eccentricity solutions ( $r$  ranges between  $-0.126$  and  $-0.154$ ).

We emphasize that these correlation coefficients have been calculated after tuning to the 405-kyr eccentricity component only. The differences in correlation coefficient are therefore related to differences in the nature of the 100-kyr and 2.4-Myr eccentricity cycles in the different eccentricity solutions for this interval. As expected, the correlation between the U1514 log(Ca/Fe) record and the full La2010c eccentricity solution increases significantly ( $r = -0.302$ ) after direct tuning. The correlation for the interval between 56 and 50 Ma remains weaker than the correlation between Ca/Fe and different astronomical solutions for the interval after 50 Ma ( $r = -0.370$  for La10c). Exploring the entire solution space for eccentricity in the early Paleogene may provide further improvement or constraints for eccentricity solutions in the early Eocene.

#### 4.4. Astronomically forced paleoenvironmental change in the Mentelle Basin during the Eocene

The rapid drop in Ca/Fe from the lower to the middle Eocene around 49 Ma is linked with a decrease in the sedimentation rate from ~1 cm/kyr to ~0.7 cm/kyr, except between 47.8 and 49 Ma, when the sedimentation rate averages ~1.6 cm/kyr (Fig. 3). The link between decreasing Ca/Fe ratios and sedimentation rates indicates reduced carbonate productivity or shallowing of the carbonate compensation depth (CCD). However, the latter seems implau-



sible, as the Indian Ocean CCD deepens across the early to middle Eocene transition (Van Andel, 1975). Hence, we explain the decrease in  $\text{CaCO}_3$  from the lower to the middle Eocene as a decrease in carbonate productivity associated with cooling surface waters.

The U1514 bulk sediment  $\delta^{18}\text{O}$  record supports cooling of surface waters in the Mentelle Basin from 50.8 Ma onwards, concurrent with Southern Hemisphere deep-water cooling at Site 702 (Katz and Miller, 1991). This is notably earlier than the majority of other deep and surface temperature records, which show the inception of cooling at  $\sim 49$  Ma (Bijl et al., 2009, 2013; Hollis et al., 2012; Mudelsee et al., 2014; Inglis et al., 2015). Thus, local surface temperatures in the Mentelle Basin appear to be decoupled from global ocean temperature trends throughout the long-term middle Eocene cooling (Fig. 1H). The cooling at U1514 ceases at  $\sim 47$  Ma, much earlier than the global Eocene deep-sea cooling. One possibility to explain the relatively early cessation of the cooling signal observed at Site U1514 is the initiation of the proto-Leeuwin Current during the middle Eocene (McGowran et al., 1997; Jackson et al., 2019) transporting warm water from low latitudes into the Mentelle Basin.

Another intriguing correlation is that the timing of decreasing carbonate deposition in the Mentelle Basin at 49 Ma coincides with the earliest estimates for a southern opening of the Tasmanian Gateway (i.e., south of the South Tasman Rise) (Bijl et al., 2013), which would have caused regional to global scale reorganization of ocean circulation that certainly would have affected the Mentelle Basin. This work will act as the solid ground for future studies that aim at unraveling the precise paleoclimatic and paleoceanographic history of the basin.

## 5. Conclusions

The U1514 sedimentary archive from the Mentelle Basin offshore southwest Australia includes a 16-million-year long history that illuminates the effects of astronomical forcing throughout the Eocene in the region. We used these deep-sea sediments for the construction of a detailed astrochronology for the early to middle Eocene. The astronomical forcing signature is expressed in lithological variability between carbonate-poor nannofossil chalks and nannofossil-rich claystone, and consists of a mixed imprint of obliquity and eccentricity. The strong expression of minima in the 2.4-Myr eccentricity cycle (nodes) at Site U1514 allowed for a robust anchoring of our middle Eocene cyclostratigraphic framework in absolute time.

Site U1514 manifests a comprehensive series of early Eocene hyperthermals, which we correlated with Atlantic deep-sea sites and Italian land sections. In other words, U1514 holds a single-site chemostratigraphic backbone for the lower to middle Eocene, well suited for global correlation.

We apply Site U1514 as a third opinion in the discussion between two competing timescales for the middle Eocene (Westerhold and Röhl, 2013; Westerhold et al., 2015; Boulila et al., 2018). The comparison between Indian Ocean Site U1514 and Atlantic Sites 702, 1260, 1263 suggests no sign of hiatuses at the latter sites. Hence, we cannot endorse Boulila et al.'s (2018) hypothesis to explain the differences between the competing timescales.

Finally, Site U1514 demonstrates a regime shift in carbonate deposition around 49 Ma, with a decrease in carbonate productivity and a decrease in average sedimentation rates. Interestingly, the timing of this shift in depositional characteristics coincides with the oldest estimates ( $\sim 49$ –50 Ma) for the southern opening of the Tasmanian Gateway. Future paleoceanographic studies of the U1514 sedimentary archive will further explore the possible link between ocean gateway opening and oceanographic changes in the Mentelle Basin.

## Acknowledgements

This research used samples and data provided by the International Ocean Discovery Program (IODP). M.V., DDV. and H.P. were funded by ERC Consolidator Grant “EarthSequencing” (Grant Agreement No. 617462). S.J.B. was funded by NERC UK-IODP grant NE/R012350/1. K.M.E. and E.H. were funded by NERC grant NE/R012490/1. M.M. was funded by CNRS. K.B. acknowledges support from the National Science Foundation (OCE – 1326927).

## Appendix A. Supplementary material

Supplementary material related to this article can be found online at <https://doi.org/10.1016/j.epsl.2019.115865>.

## References

- Anagnostou, E., John, E.H., Edgar, K.M., Foster, G.L., Ridgwell, A., Inglis, G.N., Pancost, R.D., Lunt, D.J., Pearson, P.N., 2016. Changing atmospheric  $\text{CO}_2$  concentration was the primary driver of early Cenozoic climate. *Nature* 533, 380–384.
- Baddouh, M.B., Meyers, S.R., Carroll, A.R., Beard, B.L., Johnson, C.M., 2016. Lacustrine  $^{87}\text{Sr}/^{86}\text{Sr}$  as a tracer to reconstruct Milankovitch forcing of the Eocene hydrologic cycle. *Earth Planet. Sci. Lett.* 448, 62–68.
- Berger, A., Loutre, M.-F., 1991. Insolation values for the climate of the last 10 million years. *Quat. Sci. Rev.* 10, 297–317.
- Bijl, P.K., Bendle, J.A.P., Bohaty, S.M., Pross, J., Schouten, S., Tauxe, L., Stickley, C.E., McKay, R.M., Röhl, U., Olney, M., Sluijs, A., Escutia, C., Brinkhuis, H., Scientists, E., 2013. Eocene cooling linked to early flow across the Tasmanian Gateway. *Proc. Natl. Acad. Sci. USA* 110, 9645–9650.
- Bijl, P.K., Schouten, S., Sluijs, A., Reichert, G.-J., Zachos, J.C., Brinkhuis, H., 2009. Early palaeogene temperature evolution of the southwest Pacific Ocean. *Nature* 461, 776–779.
- Boulila, S., Vahlenkamp, M., De Vleeschouwer, D., Laskar, J., Yamamoto, Y., Pälike, H., Turner, S.K., Sexton, P.F., Westerhold, T., Röhl, U., 2018. Towards a robust and consistent middle Eocene astronomical timescale. *Earth Planet. Sci. Lett.* 486, 94–107.
- Cande, S.C., Kent, D.V., 1995. Revised calibration of the geomagnetic polarity timescale for the Late Cretaceous and Cenozoic. *J. Geophys. Res., Solid Earth* 100 (B4), 6093–6095.
- Cramer, B.S., Wright, J.D., Kent, D.V., Aubry, M.P., 2003. Orbital climate forcing of  $\delta^{13}\text{C}$  excursions in the late Paleocene–early Eocene (chrons C24n–C25n). *Paleoceanography* 18.
- De Vleeschouwer, D., Vahlenkamp, M., Crucifix, M., Pälike, H., 2017. Alternating Southern and Northern Hemisphere climate response to astronomical forcing during the past 35 m.y. *Geology* 45, 375–378.
- Dickens, G.R., O’Neil, J.R., Rea, D.K., Owen, R.M., 1995. Dissociation of oceanic methane hydrate as a cause of the carbon isotope excursion at the end of the Paleocene. *Paleoceanogr. Paleoclimatol.* 10, 965–971.
- Dinarès-Turell, J., Martínez-Braceras, N., Payros, A., 2018. High-resolution integrated cyclostratigraphy from the Oyambre section (Cantabria, N Iberian Peninsula): constraints for orbital tuning and correlation of middle Eocene Atlantic Deep-Sea Records. *Geochem. Geophys. Geosyst.* 19, 787–806.
- Drury, A.J., Kotov, S., Rochholz, F., Wilkens, R., Pälike, H., 2018. Uniform, Rapid, Open Access Database for Shipboard IODP/ODP/DSDP Images. AGU, Washington, DC.
- Ebisuzaki, W., 1997. A method to estimate the statistical significance of a correlation when the data are serially correlated. *J. Climate* 10, 2147–2153.
- Fienga, A., Laskar, J., Kuchynka, P., LePoncin-Lafitte, C., Manche, H., Gastineau, M., 2009. Gravity tests with INPOP planetary ephemerides. In: *Proceedings of the International Astronomical Union*, vol. 5, pp. 159–169.
- Fienga, A., Laskar, J., Kuchynka, P., Manche, H., Desvignes, G., Gastineau, M., Cognard, I., Theureau, G., 2011. The INPOP10a planetary ephemeris and its applications in fundamental physics. *Celest. Mech. Dyn. Astron.* 111 (3), 363.
- Francescone, F., Lauretano, V., Bouligand, C., Moretti, M., Sabatino, N., Schrader, C., Catanzariti, R., Hilgen, F., Lanci, L., Turtù, A., 2018. A 9 million-year-long astrochronological record of the early–middle Eocene corroborated by seafloor spreading rates. *Geol. Soc. Am. Bull.* 131, 499–520.
- Galeotti, S., Moretti, M., Sabatino, N., Sprovieri, M., Ceccatelli, M., Francescone, F., Lanci, L., Lauretano, V., Monechi, S., 2017. Cyclochronology of the Early Eocene carbon isotope record from a composite Contessa Road-Bottaccione section (Gubbio, central Italy). *Newsl. Stratigr.* 50, 231–244.
- Galeotti, S., Sprovieri, M., Rio, D., Moretti, M., Francescone, F., Sabatino, N., Fornaciari, E., Giusberti, L., Lanci, L., 2019. Stratigraphy of early to middle Eocene hyperthermals from Possagno (Southern Alps, Italy) and comparison with global carbon isotope records. *Palaeogeogr. Palaeoclimatol. Palaeoecol.* 527, 39–52.
- Gouhier, T., Grinstead, A., Simko, V., 2016. biwavelet: conduct univariate and bivariate wavelet analyses (Version 0.20.10).

- Gradstein, F.M., Ogg, J.G., Schmitz, M., Ogg, G., 2012. The Geologic Time Scale 2012. Elsevier.
- Hays, J., Imbrie, J., Shackleton, N., 1976. Variations in the Earth's orbit: pacemaker of the ice ages. *Science* 194, 1121–1132.
- Hilgen, F.J., Kuiper, K.F., Lourens, L.J., 2010. Evaluation of the astronomical time scale for the Paleocene and earliest Eocene. *Earth Planet. Sci. Lett.* 300, 139–151.
- Hinnov, L., Hilgen, F., 2012. Cyclostratigraphy and astrochronology. In: *The Geologic Time Scale*. Elsevier, pp. 63–83.
- Hollis, C.J., Taylor, K.W.R., Handley, L., Pancost, R.D., Huber, M., Creech, J.B., Hines, B.R., Crouch, E.M., Morgans, H.E.G., Crampton, J.S., Gibbs, S., Pearson, P.N., Zachos, J.C., 2012. Early Paleogene temperature history of the Southwest Pacific Ocean: reconciling proxies and models. *Earth Planet. Sci. Lett.* 349–350, 53–66.
- Huber, B.T., Hobbs, R.W., Bogus, K.A., Batenburg, S.J., Brumsack, H.-J., Do Monte Guerra, R.E., Edgar, K.M., Edvardson, T., Harry, D.L., Hasegawa, T., Haynes, S.J., Jiang, T., Jones, M.M., Kuroda, J., Lee, E.Y., Li, Y.-X., MacLeod, K.G., Maritati, A., Martinez, M., O'Connor, L.K., Petrizzo, M.R., Quan, T.M., Richter, C., Riquier, L., Tagliaro, G.T., Garcia Tejada, M.L., Wainman, C.C., Watkins, D.K., White, L.T., Wolfgring, E., Xu, Z., 2019. Site U1514. In: Hobbs, R.W., Huber, B.T., Bogus, K.A., the Expedition 369 Scientists (Eds.), *Australia Cretaceous Climate and Tectonics. Proceedings of the International Ocean Discovery Program*, vol. 369. College Station, TX (International Ocean Discovery Program).
- Inglis, G.N., Farnsworth, A., Lunt, D., Foster, G.L., Hollis, C.J., Pagani, M., Jardine, P.E., Pearson, P.N., Markwick, P., Galsworthy, A.M., 2015. Descent toward the icehouse: Eocene sea surface cooling inferred from GDGT distributions. *Paleoceanography* 30, 1000–1020.
- Jackson, C.A., Magee, C., Hunt-Stewart, E.R., 2019. Cenozoic contourites in the eastern Great Australian Bight, offshore southern Australia: implications for the onset of the Leeuwin Current. *J. Sediment. Res.* 89, 199–206.
- Katz, M.E., Miller, K.G., 1991. Early Paleogene benthic foraminiferal assemblage and stable isotope composition in the southern ocean. In: *Proc. Ocean Drill. Program Sci. Results*, vol. 114, pp. 481–516.
- Kennett, J.P., Stott, L.D., 1991. Abrupt deep-sea warming, palaeoceanographic changes and benthic extinctions at the end of the Palaeocene. *Nature* 353, 225.
- Laskar, J., Fienga, A., Gastineau, M., Manche, H., 2011. La2010: a new orbital solution for the long-term motion of the Earth. *Astron. Astrophys.* 532, A89.
- Laskar, J., Robutel, P., Joutel, F., Gastineau, M., Correia, A., Levrard, B., 2004. A long-term numerical solution for the insolation quantities of the Earth. *Astron. Astrophys.* 428, 261–285.
- Lauretano, V., Hilgen, F., Zachos, J., Lourens, L., 2016. Astronomically tuned age model for the early Eocene carbon isotope events: a new high-resolution  $\delta^{13}\text{C}$  benthic record of ODP Site 1263 between ~49 and ~54 Ma. *Newsl. Stratigr.* 49, 383–400.
- Lauretano, V., Littler, K., Polling, M., Zachos, J., Lourens, L., 2015. Frequency, magnitude and character of hyperthermal events at the onset of the Early Eocene Climatic Optimum. *Clim. Past* 11, 1313–1324.
- Littler, K., Röhl, U., Westerhold, T., Zachos, J.C., 2014. A high-resolution benthic stable-isotope record for the South Atlantic: implications for orbital-scale changes in Late Paleocene–Early Eocene climate and carbon cycling. *Earth Planet. Sci. Lett.* 401, 18–30.
- Lourens, L.J., Sluijs, A., Kroon, D., Zachos, J.C., Thomas, E., Röhl, U., Bowles, J., Raffi, I., 2005. Astronomical pacing of late Palaeocene to early Eocene global warming events. *Nature* 435, 1083–1087.
- Ma, C., Meyers, S.R., Sageman, B.B., 2017. Theory of chaotic orbital variations confirmed by Cretaceous geological evidence. *Nature* 542, 468.
- McGowan, B., Li, Q., Cann, J., Padley, D., McKirdy, D.M., Shafik, S., 1997. Biogeographic impact of the Leeuwin Current in southern Australia since the late middle Eocene. *Palaeogeogr. Palaeoclimatol. Palaeoecol.* 136, 19–40.
- Meyers, S.R., 2014. *astrochron: An R Package for Astrochronology*, <http://cran.r-project.org/package=astrochron>.
- Mudelsee, M., Bickert, T., Lear, C.H., Lohmann, G., 2014. Cenozoic climate changes: a review based on time series analysis of marine benthic  $\delta^{18}\text{O}$  records. *Rev. Geophys.* 52, 333–374.
- Ogg, J., Smith, A., 2005. The geomagnetic polarity time scale. In: Gradstein, F., Ogg, J., Smith, A. (Eds.), *A Geologic Time Scale 2004*. Cambridge University Press, Cambridge, pp. 63–86.
- Pälike, H., Laskar, J., Shackleton, N.J., 2004. Geologic constraints on the chaotic diffusion of the solar system. *Geology* 32, 929–932.
- Pälike, H., Norris, R.D., Herrle, J.O., Wilson, P.A., Coxall, H.K., Lear, C.H., Shackleton, N.J., Tripathi, A.K., Wade, B.S., 2006. The heartbeat of the oligocene climate system. *Science* 314, 1894–1898.
- Sexton, P.F., Norris, R.D., Wilson, P.A., Pälike, H., Westerhold, T., Röhl, U., Bolton, C.T., Gibbs, S., 2011. Eocene global warming events driven by ventilation of oceanic dissolved organic carbon. *Nature* 471, 349.
- Shanmugam, G., 2017. The contourite problem. In: *Sediment Provenance*. Elsevier, pp. 183–254.
- Stap, L., Lourens, L.J., Thomas, E., Sluijs, A., Bohaty, S., Zachos, J.C., 2010. High-resolution deep-sea carbon and oxygen isotope records of Eocene Thermal Maximum 2 and H<sub>2</sub>. *Geology* 38, 607–610.
- Thomson, D.J., 1982. Spectrum estimation and harmonic analysis. *Proc. IEEE* 70, 1055–1096.
- Torrence, C., Compo, G.P., 1998. A practical guide to wavelet analysis. *Bull. Am. Meteorol. Soc.* 79, 61–78.
- Tsukui, K., Clyde, W.C., 2012. Fine-tuning the calibration of the early to middle Eocene geomagnetic polarity time scale: paleomagnetism of radioisotopically dated tuffs from Laramide foreland basins. *Bulletin* 124 (5–6), 870–885.
- Turner, S.K., Sexton, P.F., Charles, C.D., Norris, R.D., 2014. Persistence of carbon release events through the peak of early Eocene global warmth. *Nat. Geosci.* 7, 748–751.
- Vahlenkamp, M., Niezgodzki, I., De Vleeschouwer, D., Bickert, T., Harper, D., Kirtland Turner, S., Lohmann, G., Sexton, P., Zachos, J., Pälike, H., 2018. Astronomically paced changes in deep-water circulation in the western North Atlantic during the middle Eocene. *Earth Planet. Sci. Lett.* 484, 329–340.
- Van Andel, T.H., 1975. Mesozoic/Cenozoic calcite compensation depth and the global distribution of calcareous sediments. *Earth Planet. Sci. Lett.* 26, 187–194.
- Van Peer, T.E., Xuan, C., Lippert, P.C., Liebrand, D., Agnini, C., Wilson, P.A., 2017. Extracting a detailed magnetostratigraphy from weakly magnetized, Oligocene to early Miocene sediment drifts recovered at IODP Site U1406 (Newfoundland margin, northwest Atlantic Ocean). *Geochem. Geophys. Geosyst.* 18, 3910–3928.
- Westerhold, T., Röhl, U., 2013. Orbital pacing of Eocene climate during the Middle Eocene Climate Optimum and the chron C19r event: missing link found in the tropical western Atlantic. *Geochem. Geophys. Geosyst.* 14, 4811–4825.
- Westerhold, T., Röhl, U., Frederichs, T., Agnini, C., Raffi, I., Zachos, J.C., Wilkens, R.H., 2017. Astronomical calibration of the Ypresian time scale: implications for seafloor spreading rates and the chaotic behaviour of the solar system. *Clim. Past* 13, 1129–1152.
- Westerhold, T., Röhl, U., Frederichs, T., Bohaty, S., Zachos, J., 2015. Astronomical calibration of the geological timescale: closing the middle Eocene gap. *Clim. Past* 11, 1181.
- Westerhold, T., Röhl, U., Laskar, J., Raffi, I., Bowles, J., Lourens, L.J., Zachos, J.C., 2007. On the duration of magnetochrons C24r and C25n and the timing of early Eocene global warming events: implications from the Ocean Drilling Program Leg 208 Walvis Ridge depth transect. *Paleoceanography* 22.
- Westerhold, T., Röhl, U., Pälike, H., Wilkens, R., Wilson, P., Acton, G., 2014. Orbitally tuned timescale and astronomical forcing in the middle Eocene to early Oligocene. *Clim. Past* 10, 955–973.
- Westerhold, T., Röhl, U., Raffi, I., Fornaciari, E., Monechi, S., Reale, V., Bowles, J., Evans, H.F., 2008. Astronomical calibration of the Paleocene time. *Palaeogeogr. Palaeoclimatol. Palaeoecol.* 257, 377–403.
- Zachos, J.C., Dickens, G.R., Zeebe, R.E., 2008. An early Cenozoic perspective on greenhouse warming and carbon-cycle dynamics. *Nature* 451, 279–283.
- Zachos, J.C., Röhl, U., Schellenberg, S.A., Sluijs, A., Hodell, D.A., Kelly, D.C., Thomas, E., Nicolo, M., Raffi, I., Lourens, L.J., 2005. Rapid acidification of the ocean during the Paleocene-Eocene thermal maximum. *Science* 308, 1611–1615.
- Zeebe, R.E., 2017. Numerical solutions for the orbital motion of the Solar System over the past 100 Myr: limits and new results. *Astron. J.* 154, 193.